

## PLASTICITY AND FRACTURE AT THE NANOSCALES

# Dislocation spreading and ductile–to–brittle transition in post-irradiated ferritic grains: Investigation of grain size and grain orientation effect by means of 3D dislocation dynamics simulations

Yang Li<sup>1,a)</sup>, Christian Robertson<sup>2,b)</sup>, Xianfeng Ma<sup>3</sup>, Biao Wang<sup>3</sup><sup>1</sup>DEN-Service de Recherches Métallurgiques Appliquées, CEA, Université Paris-Saclay, Gif-sur-Yvette 91191, France; and Sino-French Institute of Nuclear Engineering and Technology, Sun Yat-sen University, Zhuhai 519082, China<sup>2</sup>DEN-Service de Recherches Métallurgiques Appliquées, CEA, Université Paris-Saclay, Gif-sur-Yvette 91191, France<sup>3</sup>Sino-French Institute of Nuclear Engineering and Technology, Sun Yat-sen University, Zhuhai 519082, China

a)Address all correspondence to these authors. e-mail: yang.li@cea.fr

b)e-mail: christian.robertson@cea.fr

Received: 1 October 2018; accepted: 25 March 2019

Post-irradiation plastic strain spreading in ferritic grains is investigated by means of three-dimensional dislocation dynamics simulations, whereby dislocation-mediated plasticity mechanisms are analyzed in the presence of various disperse defect populations, for different grain size and orientation cases. Each simulated irradiation condition is then characterized by a specific “defect-induced apparent straining temperature shift” ( $\Delta$ DIAT) magnitude, reflecting the statistical evolutions of dislocation mobility. It is found that the calculated  $\Delta$ DIAT level closely matches the ductile-to-brittle transition temperature shift ( $\Delta$ DBTT) associated with a given defect dispersion, characterized by the (average) defect size  $D$  and defect number density  $N$ . The noted  $\Delta$ DIAT/ $\Delta$ DBTT correlation can be explained based on plastic strain spreading arguments and applicable to many different ferritic alloy compositions, at least within the range of simulation conditions examined herein. This systematic study represents one essential step toward the development of a fully predictive, dose-dependent fracture model, adapted to polycrystalline ferritic materials.

## Introduction

The mechanical properties of ferritic materials are subjected to detrimental dose-dependent evolutions, including embrittlement, swelling, hardening, and radiation-induced segregations. These evolutions represent an important life-limiting factor for various types of nuclear installations [1, 2, 3, 4]. Ferritic materials are characterized by a well-defined ductile-to-brittle transition (DBT), in both irradiated and non-irradiated conditions [5, 6, 7, 8, 9]. Usual surveillance practices include the DBT temperature assessment of the reactor pressure vessel (RPV) steel. Such evaluation involves the destructive testing of a fixed number of macroscopic specimens inserted in surveillance capsules located near the RPV inner wall prior to the initial reactor start-up. The surveillance specimens are taken out-of-pile at a selected periodicity (a few years, typically) and then handled, tested, and disposed of in hot cell facilities [10,

11, 12]. Although reliable, this conventional approach is time-consuming and extremely costly and lacks flexibility.

In that context, it is highly desirable to develop and apply supporting evaluation methods, preferably based on numerical simulation and nondestructive observation techniques, like EBSD analysis [13], small-angle neutron scattering (SANS) measurements [14, 15], or X-ray submicron diffraction methods [16, 17, 18]. Such approach could then help optimizing the existing surveillance programs, while providing valuable complementary information regarding the material degradation causes. Progress toward the said objectives can be achieved by taking advantage of recent numerical simulation results [19, 20], addressing post-irradiation plastic strain spreading at the scale of ferritic grains.

The exposure of metallic materials to neutron irradiation flux results in the progressive accumulation of radiation-induced defect clusters, mostly in the form of dislocation loops.

These defect clusters can then strongly interact with dislocation-mediated plasticity mechanisms according to transmission electron microscopy (TEM) observations [21, 22], molecular dynamics (MD) [23, 24], and dislocation dynamics (DD) simulation analysis [25, 26, 27, 28]. It is important to note that the DBT of ferritic materials is concurrent with and generally depends on the temperature-dependent mobility of screw dislocations, based on thermally activated slip and cross-slip theory [29, 30, 31]. Analysis of the dislocation-mediated plasticity mechanisms has shown that [19, 20]

- (i) Both the straining temperature and the defect dispersions primarily impact the effective screw dislocation mobility.
- (ii) The defect dispersions impact the effective dislocation mobility depending on the defect size and defect number densities.
- (iii) The defect-induced changes can be expressed in terms of a quantitative scalar indicator called the “defect-induced apparent straining temperature shift” (noted  $\Delta$ DIAT).

Our goal in this work is to evaluate the grain size and grain orientation effect on  $\Delta$ DIAT evolutions using three-dimensional DD simulations. This evaluation is regarded as an essential step toward developing a fully predictive model, applicable at the scale of representative (macroscopic) grain aggregates and then macroscopic specimens [32]. This particular study is adapted to Fe–2.25% Cr grains taken as a model ferritic system, for which all the required data are available in the open literature (see also “Dislocation stress-velocity rules”), as far as dislocation mobility is concerned [33].

The present article thus includes the following core sections. The adopted methodology is presented in “Investigation methods”, namely the dislocation mobility rules (“Dislocation stress-velocity rules”), the different DD simulation setups, and dislocation/defect interaction treatment (“Grain setups and dislocation/defect interaction implementation”). The defect-dependent evolutions of the effective dislocation mobility are evaluated based on  $\Delta$ DIAT, as presented in “Defect induced changes of effective dislocation mobility and DIAT shift concept”. “Results and discussion” presents the various  $\Delta$ DIAT trends associated with various simulation conditions and setups. The grain size and grain orientation effects are presented in “Grain size effect on plastic strain spreading” and “Grain orientation effect”, respectively. Relations between the present simulation results and corresponding post-irradiation ductile-to-brittle transition temperature shifts ( $\Delta$ DBTT) are then further examined and discussed. In certain irradiation conditions, the DIAT shift level is comparable to the  $\Delta$ DBTT (see “Grain size and orientation effect on  $\Delta$ DIAT and dislocation microstructures”). This correlation is interpreted in

“The  $\Delta$ DIAT versus  $\Delta$ DBTT correlation”, based on both experimental evidence and theoretical arguments.

## Results and discussion

### Grain size effect on plastic strain spreading

#### Effect on the mechanical response and dislocation accumulation rate

The stress–strain responses of 1 and 2  $\mu\text{m}$  defect-free grains are shown side by side in Fig. 1(a). The initial applied stress level (where  $\epsilon_p < 2 \times 10^{-4}$ ) is proportional to  $1/\sqrt{D_g}$ , i.e., consistent with the well-known Hall–Petch effect, associated with the internal stress landscape, where the dislocations store at the grain boundaries. The work-hardening rate is limited, in agreement with the stress–strain response of polycrystalline BCC metals [33]. The mean applied stress level is consistent with the observed mobile dislocation densities [see Fig. 1(b)], given the selected (controlled) plastic strain rate conditions and the adopted stress–velocity rules. The dislocation density accumulation rate is linear with the cumulated plastic strain, in both Grain

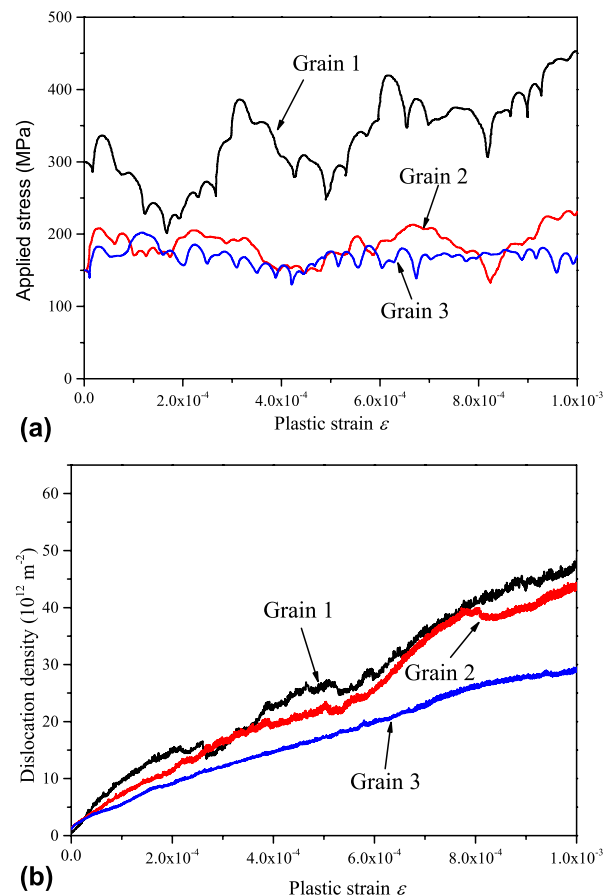


**Figure 1:** Plastic strain spreading in defect-free Grain 1, Grain 2, and Grain 3 simulation setups. (a) Stress–strain response. (b) Dislocation density evolution with cumulated plastic strain. Grain 1, Grain 2, and Grain 3 labels are defined in Table III.

1 and Grain 2 cases. At a fixed plastic strain level, the dislocation density is slightly lower in Grain 2 than in Grain 1, despite the relatively large applied stress gap between the two cases. A comparable effect is observed in MD simulations [34] using similar boundary conditions as specified in “Investigation methods”. In the present DD simulations, the dislocation structures take the form of individual shear bands, whose number density increases with the increasing strain level and disperse defect number density [27, 35, 36]. Dislocation multiplication inside individual shear bands is due to the formation of dislocation sources (in the form of open loops) and very active cross-slip [27, 37]. In these conditions, it can be shown that the actual shear band thickness and spacing are consistent with the internal stress field evolutions [38, 39]. In any case, the observed grain size effect on the dislocation density accumulation rate is in good agreement with earlier DD simulation results and direct experimental evidence [27, 28, 35, 36, 39].

The (average) applied stress level is dose dependent (not shown), i.e., increases with the defect number density [19, 33]. This effect mainly depends on the dislocation mobility rules and dislocation/facet interaction mechanisms that are likewise grain size independent.

### Effect on effective dislocation mobility and $\Delta$ DIAT

The DIAT shift amplitude corresponding to each simulation case is then calculated using Eqs. (4) and (5) and plotted in Fig. 2 (solid symbols).

For a fixed grain size, the DIAT shift increases with the defect size and number density up to a specific, case-dependent saturation level. In Grain 2 and  $D = 25$  nm case, for example, the  $\Delta$ DIAT level saturates at 95 K for a defect number density  $N > 10^{21} \text{ m}^{-3}$ . For a fixed irradiation condition, larger grain size induces higher  $\Delta$ DIAT, especially with small defect number density. In  $D = 25$  nm case, for instance,  $\Delta$ DIAT increases from 38 K ( $D_g = 1 \mu\text{m}$ ) to 71 K ( $D_g = 2 \mu\text{m}$ ) at  $5 \times 10^{20} \text{ m}^{-3}$  defect number density. According to Fig. 1, increasing the grain size (at fixed strain rate) induces lower applied stress and dislocation accumulation rate, which means dislocation propagations in larger grain become much easier yielding more mobile dislocations. Therefore, the influence of defect dispersions in Grain 2 is relatively more important than that in Grain 1 in terms of statistical dislocation mobility, which finally results in a larger  $\Delta$ DIAT amplitude. The grain size effect is significantly smaller for higher defect densities [see Fig. 2(b)], where the dislocation/defect interaction rate is dominant, in terms of dislocation multiplication mechanism.

### Grain orientation effect

#### Effect on plastic strain spreading

The grain orientation effect is evaluated by comparing the DD simulation results associated with Grain 2 and 3 setups (see

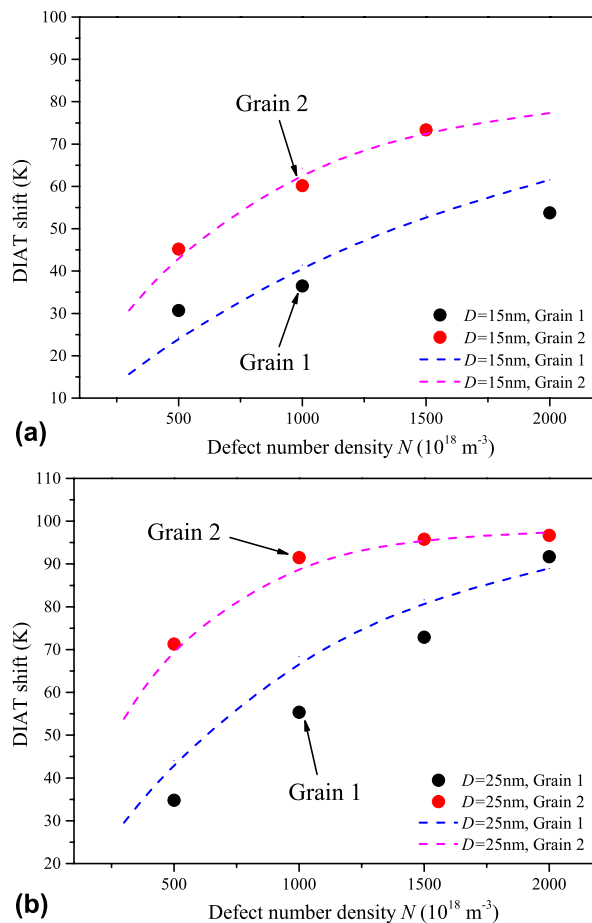


**Figure 2:**  $\Delta$ DIAT evolutions for different defect number densities in Grain 1 and Grain 2 simulation setups. Grain size effect for different defect number density cases: (a) defect size  $D = 15$  nm and (b) defect size  $D = 25$  nm. Solid symbols: DD simulation results using Eq. (5); dashed lines: Eq. (1) prediction for corresponding  $D$  and  $N$  inputs. Adjustment of  $\Delta$ DIAT data with analytical Eq. (1) is further discussed in “Discussion.”

section “Grain setups and dislocation/defect interaction implementation”). The applied stress and dislocation density evolutions with plastic strain in defect-free case are shown in Figs. 1(a) and 1(b).

The significant grain orientation dependence hereby is due to decreased activity in the first slip system (SS). In the second SS, however, the dislocation density is almost unchanged for the two tested grain orientations (not shown). It is understood that these evolutions closely reflect the Schmid factors evolutions indicated in Table IV. Obtaining the exact form of the grain orientation dependence on  $\Delta$ DIAT involves further theoretical developments to be presented in a separate paper. In principle, however, a grain orientation yielding a lower Schmid factor (in either the primary or cross-slip systems) is also associated with a smaller internal stress field and finer shear bands (see also Fig. 4 and Ref. 38). This interpretation is validated by the simulation results to be presented in the next sections.

### Effect on effective dislocation mobility and $\Delta$ DIAT

The grain orientation effect on the  $\Delta$ DIAT evolutions is presented in Fig. 3, showing a similar trend as in Fig. 2. However, the  $\Delta$ DIAT level is systematically lower in the  $z = (\bar{1}54)$  oriented Grain 3 than in the  $z = (100)$  oriented Grain 2. In the  $D = 25$  nm cases,  $\Delta$ DIAT achieves a saturation level for about  $N = 10^{21} \text{ m}^{-3}$  in Grain 2 and  $N > 1.5 \times 10^{21} \text{ m}^{-3}$  in Grain 3. It is interesting to note that for a fixed defect size, the saturation level is mostly independent of the grain orientation. This situation especially applies to large defect number density cases, where the dislocation multiplication is dominated by the dislocation/defect interactions.

### Discussion

#### Grain size and orientation effect on $\Delta$ DIAT and dislocation microstructures

All the  $\Delta$ DIAT results presented in “Grain size effect on plastic strain spreading” and “Grain orientation effect” can be described (i.e., adjusted) using the following semianalytical, dose-dependent expression (dashed lines in Figs. 2 and 3):

$$\Delta\text{DIAT} = \Delta T_{\text{max}} \left( 1 - \exp\left(-\frac{D}{\lambda}\right) \right) \left( 1 - \exp(-d^2 DN) \right) \quad (1)$$

where  $D$  (in m) is the defect size and  $N$  (in  $\text{m}^{-3}$ ) the defect number density. The exponential terms in Eq. (1) actually scale with the characteristic evolutions of the internal stress field, as shown in section 3.4 of Ref. 19. Equation (1) includes three independent scaling parameters:  $\Delta T_{\text{max}} = 110$  K is a reference temperature shift;  $\lambda \sim 11$  nm is a reference gliding distance, and  $d$  is the thickness of the strain-induced shear bands. The

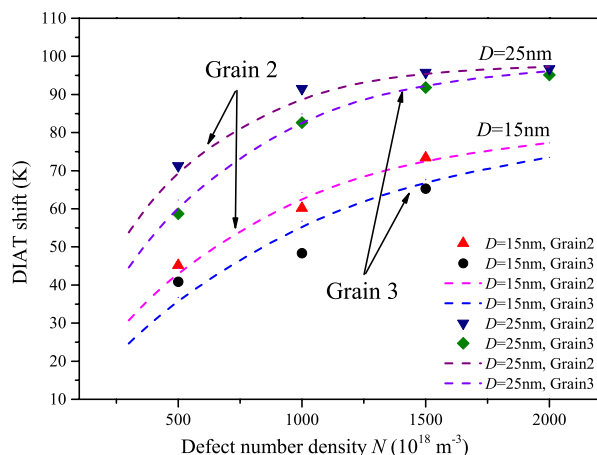


**Figure 3:**  $\Delta$ DIAT evolutions using Grain 2 and Grain 3 simulation setups for various defect dispersion cases: grain orientation effect. Solid symbols: DD simulation results using Eq. (5); dashed lines: Eq. (1) prediction for corresponding  $D$  and  $N$  inputs. Adjustment of  $\Delta$ DIAT data with Eq. (1) is further discussed in “Discussion.”

reference temperature shift  $\Delta T_{\text{max}}$  can be estimated assuming coplanar dislocation interaction with hard (non-shearable) disperse defects. In stress-controlled deformation conditions,  $\tau_1^* \approx \tau_0^* + \Delta\tau_{\text{Orowan}}$ , where  $\Delta\tau_{\text{Orowan}}$  is calculated using the Scattergood and Bacon expression [35] with saturation value  $N = 2 \times 10^{22} \text{ m}^{-3}$  for  $D = 16$  nm (see [2] for example). Inserting  $\tau_1^*$  in Eq. (2), putting the corresponding  $v_1$  in Eq. (4) and then solving for  $T_1$  yields  $(T_1 - T_0) = \Delta T_{\text{max}} \sim 110$  K. Distance  $\lambda$  is the average integrated free glide path of screw dislocations between consecutive glide plane changes due to cross-slip mechanism (please refer again to Ref. 19). We found that  $\lambda$  is grain size and grain orientation independent at least in the conditions of this study.

In practice, Fig. 2 data can be adjusted using Eq. (1) by varying the shear band thickness parameter, namely by using  $d = 320$  nm with Grain 2 data and  $d = 220$  nm with Grain 1 data (see Table I). Similarly, Fig. 3 data can be adjusted using Eq. (1) with  $d = 280$  nm for Grain 3 data and  $d = 320$  nm for Grain 2 data (see also Table I). The shear band thicknesses obtained by adjusting  $\Delta$ DIAT data with Eq. (1) are in any case consistent with the simulation-generated dislocation microstructures (see Fig. 4). Thicker shear bands are found in larger grains (since  $d \propto D_g^{1/2}$ ) and generate a higher DIAT shift for a given defect dispersion. Increasing the grain size indeed facilitates dislocation cross-slip, which is consistent with thicker shear bands and a more pronounced evolution of the dislocation mobility (with respect to the defect-free case). Changing the grain orientation significantly affects the  $\Delta$ DIAT level for a given grain size. This particular effect is associated with corresponding change in the applied resolved shear stress repartition, among the different SS. This effect most probably contributes to the  $\Delta$ DIAT scattering in polycrystalline aggregates.

“Grain size effect on plastic strain spreading” and “Grain orientation effect” results and their relation with the dose-dependent fracture response evolutions are examined in “The  $\Delta$ DIAT versus  $\Delta$ DBTT correlation”.

#### The $\Delta$ DIAT versus $\Delta$ DBTT correlation

The  $\Delta$ DIAT levels reported in Figs. 2 and 3 closely reflect the actual dose-dependent  $\Delta$ DBTT data associated with irradiation conditions (and materials) compatible with the present study [2, 3, 4, 5, 6, 40, 41, 42, 43, 44, 45, 46, 47]. Figure 5(a) presents

**TABLE I:** Shear band thickness parameter  $d$  estimated by adjusting Eq. (1) in  $\Delta$ DIAT simulation results. The data are consistent with  $d \propto D_g^{1/2}$ . This means, for example, that  $d(D_g = 10 \mu\text{m}) = d(D_g = 1 \mu\text{m}) \times \sqrt{10 \mu\text{m}/1 \mu\text{m}} = 220 \text{ nm} \times \sqrt{10} = 700 \text{ nm}$  (see also “The  $\Delta$ DIAT versus  $\Delta$ DBTT correlation”).

	Grain 1	Grain 2	Grain 3
Shear band thickness $d$ from Eq. (1) and DIAT shift results	220 nm	320 nm	280 nm

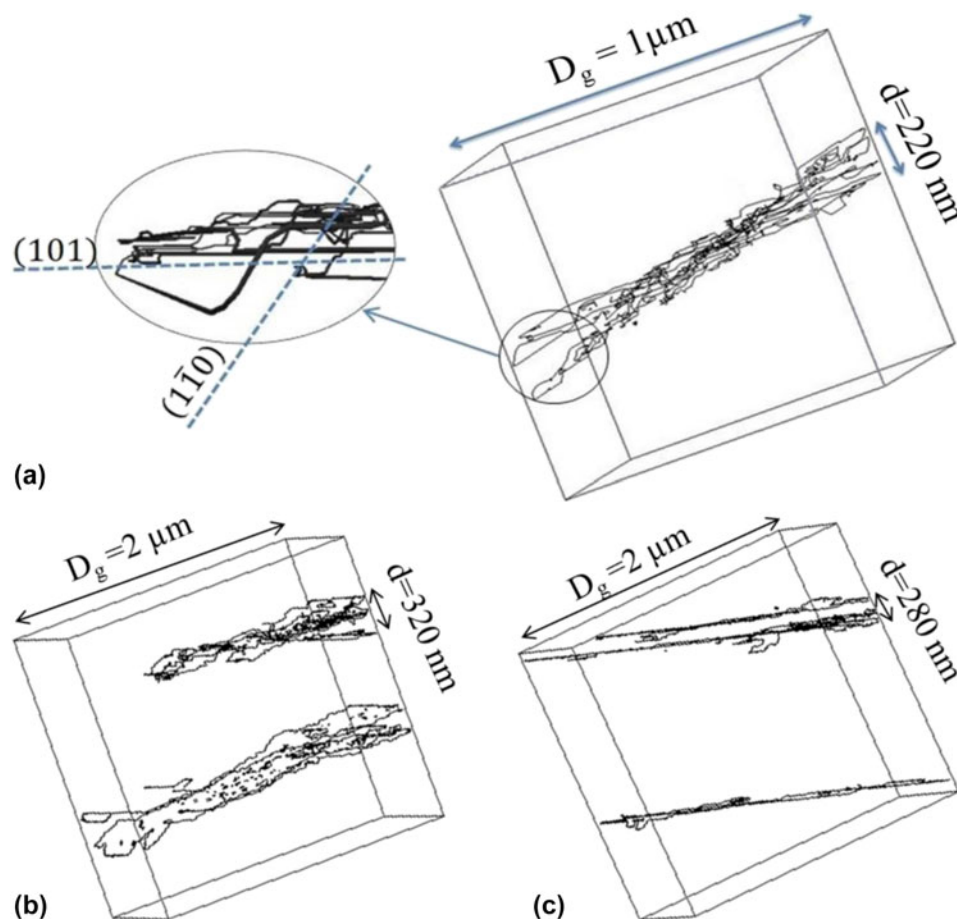


**Figure 4:** Dislocation structures at the same plastic strain level for  $N = 10^{21} \text{ m}^{-3}$  and  $D = 15 \text{ nm}$ : grain size and grain orientation effects. The defects are not shown for clarity. (a) Grain 1, (b) Grain 2, and (c) Grain 3 simulation setups (see Table III). The shear band thicknesses are consistent with the  $\Delta\text{DIAT}$ -based values calculated using Eq. (1) and reported in Table I.

the case of Fe–2.25% Cr VVER-1000 steel irradiated to different neutron doses, at two different temperatures. The  $\Delta\text{DBTT}$  data set ① corresponds to irradiation temperature  $T = 400 \text{ }^\circ\text{C}$ , neutron dose range  $10^{22}\text{--}5 \times 10^{23} \text{ m}^{-2}$  and grain size  $D_g = 10 \text{ } \mu\text{m}$  (shear band thickness  $d \sim 700 \text{ nm}$ ; see Table I caption) [42]. For a fixed irradiation temperature, the defect size is mostly dose independent, while the defect number density linearly augments with the neutron dose (or fluence) [2, 48]. The defect size  $D = 7 \text{ nm}$  and number densities  $N$  corresponding to data set ① are evaluated based on TEM observations [43]. Similarly,  $\Delta\text{DBTT}$  data set ② corresponds to irradiation temperature  $T = 288 \text{ }^\circ\text{C}$ , neutron fluence range  $7 \times 10^{23}\text{--}1.4 \times 10^{24} \text{ m}^{-2}$  and grain size  $D_g = 2 \text{ } \mu\text{m}$  (shear band thickness  $d \sim 320 \text{ nm}$ ) [44]. The defect size  $D = 5 \text{ nm}$  and number densities  $N$  associated with data set ② come from Refs. 45 and 46. The  $\Delta\text{DIAT}$  curves A and B are calculated with Eq. (1) using  $D$ ,  $d$ , and  $N$  values associated with data sets ① and ②, respectively, whereas  $\Delta T_{\text{max}} = 110 \text{ }^\circ\text{C}$  and  $\lambda = 11 \text{ nm}$  (see “Grain size and orientation effect on  $\Delta\text{DIAT}$  and dislocation microstructures”).

Interestingly, we found that Eq. (1) also applies to ferritic alloys of different Cr concentrations. Figure 5(b) presents two different Fe–9% Cr steel cases, Eurofer97 and F82H, irradiated to different neutron doses, at  $300 \text{ }^\circ\text{C}$ . The  $\Delta\text{DBTT}$  data set ③ corresponds to Eurofer97 steel, neutron doses  $0.3\text{--}2.5 \text{ dpa}$  and lath (or grain) size  $D_g = 1 \text{ } \mu\text{m}$  (shear band thickness  $d \sim 220 \text{ nm}$ ) [2]. The defect size  $D = 15 \text{ nm}$  and number densities  $N$  associated with data set ③ are taken from Ref. 2. The  $\Delta\text{DBTT}$  data set ④ corresponds to F82H steel, neutron doses  $0.2\text{--}2.5 \text{ dpa}$  and lath (or grain) size  $D_g = 2 \text{ } \mu\text{m}$  (shear band thickness  $d = 320 \text{ nm}$ ) [40]. The defect size  $D = 7 \text{ nm}$  and defect densities  $N$  corresponding to data set ④ are taken from Ref. 47. The  $\Delta\text{DIAT}$  curves C and D are calculated with Eq. (1) using  $D$ ,  $d$ , and  $N$  values associated with data sets ③ and ④, respectively (using  $\Delta T_{\text{max}} 110 \text{ }^\circ\text{C}$  and  $\lambda = 11 \text{ nm}$ , as before).

The  $\Delta\text{DIAT}$  versus  $\Delta\text{DBTT}$  equivalence reported in Fig. 5 can be rationalized as follows. Brittle fracture in ferritic materials is governed by the cleavage initiator distributions (e.g., carbide particles) [49]. This situation can be statistically treated using the weakest-link theory [50] in combination with

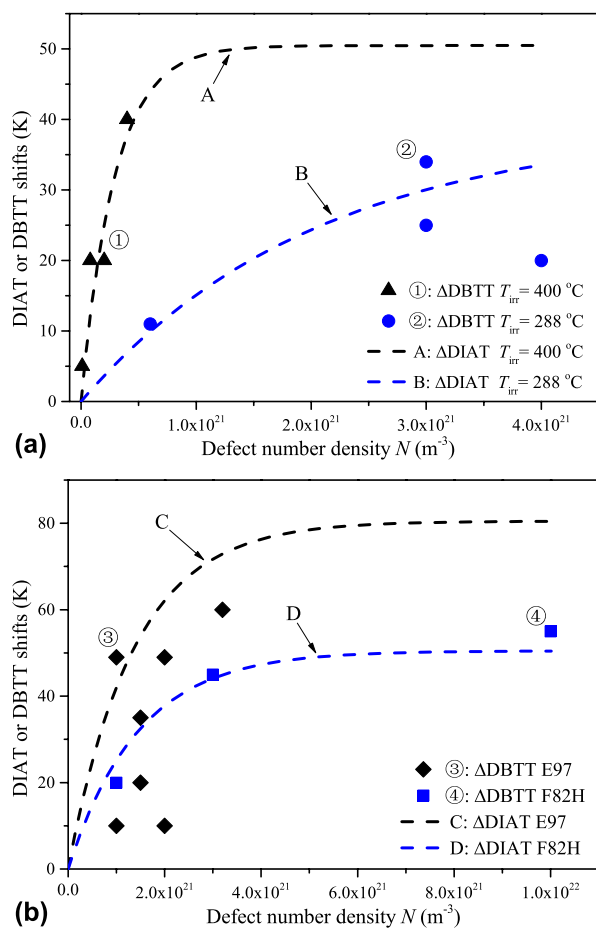


**Figure 5:** Comparison between calculated  $\Delta\text{DIAT}$  results and actual  $\Delta\text{DBTT}$  data obtained for different ferritic materials and neutron irradiation conditions. (a) Case of Fe-2.25% Cr VVER-1000 steel irradiated to different neutron doses at two different temperatures.  $\Delta\text{DBTT}$  data sets ① and ② (solid symbols) are associated with  $\Delta\text{DIAT}$  curves A and B (dashed lines), calculated using Eq. (1) with corresponding input data. (b) Case of two different Fe-9% Cr steels irradiated to different neutron doses at 300 °C: F82H and Eurofer97.  $\Delta\text{DBTT}$  data sets ③ and ④ (solid symbols) are associated with  $\Delta\text{DIAT}$  curves C and D (dashed lines), calculated using Eq. (1) with the corresponding input data.

crystal plasticity modeling [51, 52]. The fracture probability associated with a given dose level then only depends on the stress field acting on the cleavage initiators [see Eq. (7) in p. 300 of Ref. 53]. This perception is consistent with the well-known empirical correlation  $\Delta\text{DBTT} \sim \eta \Delta\sigma_{\text{applied}}$  [54], where  $\Delta\sigma_{\text{applied}}$  is the irradiation-induced increase of the yield stress and “ $\eta$ ” the proportionality factor (in K/MPa units). Likewise, we have seen that changing the grain size affects the dislocation sub-structure characteristic dimensions (see Fig. 4) and associated internal stress landscape  $\tau_{\text{int}}$ . The corresponding  $\Delta\text{DIAT}$  trends (see Figs. 2 and 3) indicate that the “ $\exp(-D/\lambda)$ ” and “ $\exp(-d^2DN)$ ” terms in Eq. (1) actually scale with subgrain  $\sigma_{\text{internal}}/\sigma_{\text{applied}}$  evolutions, which finally makes it  $\Delta\text{DIAT} \sim \theta \Delta\sigma_{\text{applied}}$  [19, 38], where “ $\theta$ ” is expressed in K/MPa units. Factor  $\eta \approx \theta$  in Fe-2.25% Cr grains and therefore  $\Delta\text{DIAT} \approx$

$\Delta\text{DBTT}$  for a broad  $\Delta\sigma_{\text{applied}}$  domain, compatible with the materials and irradiation conditions as documented in Fig. 5.

One more simulation setup, including a subgrain microcrack, has been tested in an attempt to emulate this most usual fracture initiation condition [2, 3]. We thus found that the crack-induced stress field yields no major difference in terms of  $\Delta\text{DIAT}$  magnitude: Eq. (1) is applicable without any further microcrack-related correction (unpublished results). The reader should, however, keep in mind that the current  $\Delta\text{DIAT}$  framework is exclusively based on dislocation-mediated plasticity mechanisms. This approach characterizes the brittle-ductile transition through the quantitative dislocation mobility changes associated with defect dispersion populations, regardless of the defect type (dislocation loop, vacancy loop, voids, or others) involved. In certain irradiation conditions, additional physical causes may also contribute to the dose-dependent fracture response evolutions. For example, the  $\Delta\text{DBTT}$  level is systematically higher in the presence of significant segregating element concentrations at grain boundaries and/or particle/matrix interfaces (e.g., He [40] and Chap. 6 in [55] for details). This means segregations have a distinct contribution to the DBTT shift, adding up to the plasticity mechanisms considered in “Investigation methods”. It is therefore expected that  $\Delta\text{DBTT} > \Delta\text{DIAT}$  under a certain (yet to be explored) range of irradiation conditions. Accounting for these effects entails further investigation effort by means of adapted simulation methods (e.g., the segregation effect [56]). In its current form, Eq. (1) best applies to irradiation conditions, where interfacial segregations, helium production, included particle dissolution, or grain size changes are limited, i.e., for relatively low dose and irradiation temperature conditions in ferritic steels. The limiting radiation condition specified in this section is at best indicative (dose  $< 2\text{--}3$  dpa, irradiation temperature  $T < 400^\circ\text{C}$ ), being associated with the largest disperse defect size tested herein.

## Conclusions

Grain scale plasticity is investigated using three-dimensional DD simulations adapted to ferritic materials. The effect of defect dispersions on the effective screw dislocation mobility is examined under strain rate-controlled tensile loading conditions, accounting for thermally activated mobility rules and cross-slip mechanism at 300 K. The corresponding defect-induced changes are associated with a Defect-Induced Apparent straining Temperature shift, calculated without adjusting parameters and noted “ $\Delta\text{DIAT}$ .” Analysis of the simulation trends shows that

- (1) For a given defect dispersion, the  $\Delta\text{DIAT}$  amplitude increases with the grain size, depending on the grain orientation;

- (2) The  $\Delta$ DIAT level obtained for a disperse defect size  $D$  and defect number density  $N$  case closely reflects the experimentally observed  $\Delta$ DBTT associated with exactly the same, actual  $D$  and  $N$  case;
- (3) The reported  $\Delta$ DIAT evolutions scale with the shear band thickness parameter “ $d$ ” that itself is grain size and grain orientation dependent;
- (4) The proposed  $\Delta$ DIAT indicator best applies to a dose range and irradiation temperatures, where the radiation-induced modifications of the material (segregations, inclusion, grain size changes, etc.) are minimal.

The  $\Delta$ DIAT concept is developed with a view to facilitate the prediction of dose-dependent DBT temperature shift evolutions, based on direct observation/measurement of the radiation-induced defect populations. More precisely, DBT shift evolutions can be estimated using Eq. (1) together with actual material microstructure (e.g., EBSD analysis) and radiation-induced disperse defect (e.g., SANS measurements) observation data. This approach can potentially help reducing the need for costly and time-consuming post-irradiation mechanical testing in hot cells and provide valuable complementary information, especially if used in combination with conventional surveillance techniques.

## Investigation methods

### Dislocation stress–velocity rules

DD simulations of plastic strain spreading are carried out using the TRIDIS code, where the dislocation lines are treated as discrete, orthogonal edge and screw segments [57]. These segments glide in discrete body center cubic lattice, where the lattice spacing parameter represents 10 times the Burgers vector magnitude  $b$ . Dislocation segment displacements are calculated according to applicable dislocation mobility rules. In body-center cubic metals, screw dislocation velocity is temperature and stress dependent [58, 59, 60], as

$$v_{\text{screw}} = hJX' = h \frac{8\pi(\tau^*)^2}{\mu Bh} \exp\left(-\frac{\Delta H_0}{k_B T} \left[1 - \left(\frac{\tau^*}{\tau_0}\right)^p\right]^q\right) \frac{X_\infty L}{X_\infty + L}, \quad (2)$$

where  $h$  is the Peierls valley separation, i.e., the Burgers vector magnitude  $b$  associated with the (110)[111] SS [61];  $J$  is the kink pair nucleation rate per unit dislocation length,

and  $X' = X_\infty L / (X_\infty + L)$  represents the glide distance of the kink pair before its annihilation with an opposite kink pair, propagating along a finite-length screw dislocation with length  $L$ . In the right-hand side of Eq. (2),  $B$  is the viscous drag coefficient,  $\mu$  is the shear modulus,  $k_B$  is the Boltzmann constant,  $T$  is the straining or test temperature,  $\tau^*$  is the effective resolved shear stress acting on the dislocation segment, and  $\Delta H_0$  and  $\tau_0$  are the kink pair formation energy and Peierls shear stress at 0 K, respectively. Parameters  $p$  and  $q$  are used to characterize the shape of the thermal activation barrier  $\Delta G$ , that is,  $\Delta G = \Delta H_0 [1 - (\tau^*/\tau_0)^p]^q$ . Quantity  $X_\infty$  is a reference kink pair propagation distance, corresponding to

$$X_\infty = 2 \left(\frac{v_k}{J}\right)^{1/2}, \quad (3)$$

where  $v_k = v_{\text{edge}} = \tau^* b / B$  [62, 63].

The stress- and temperature-dependent constitutive rules, together with the material-dependent parameters of Table II, enable a gradual transition of the stress–velocity response with increasing straining temperature. The corresponding stress–strain evolutions are fully consistent with mechanical response of Fe–2.25% Cr steel for the whole DBT temperature range [64, 65]. The cross-slip mechanism implemented herein is based on a specific Monte Carlo type algorithm, depending on the stress applied on the primary slip plane and the corresponding cross-slip plane (please see Refs. 27, 35, and 36 for details).

### Grain setups and dislocation/defect interaction implementation

The different DD simulation setups implemented and tested herein are listed in Table III. RPV steels usually present a multi-lath microstructure, with typical lath dimensions  $a \times 10 \times 10 \mu\text{m}^3$ . Simulating  $a \times 10 \times 10 \mu\text{m}^3$  volumes irradiated to 0.1 dpa requires handling as many as  $10^5$  defects, representing a significant computation load for small computer systems. We thereby checked that the shear band structures obtained in  $a\text{-}\mu\text{m}^3$  cubic grains are identical to those obtained in  $a \times 10 \times 10 \mu\text{m}^3$  laths, in terms of shear band thickness and mobile and stored dislocation densities (see, e.g., Fig. 10 in Ref. 36).

Additionally, direct TEM observations have shown that the strain-induced dislocations are mostly confined inside of the individual laths, up to significant macroscopic tensile strain levels, regardless of the internal coherency stresses coming from the other grains [28, 38, 39, 66]. Using impenetrable grain boundaries allows for a realistic description of intragranular

**TABLE II:** Material-dependent parameters associated with Fe–2.25% Cr grains.

$\Delta H_0$ ( $10^{-20}$ J)	$\tau_0$ (MPa)	$p$	$q$	Viscous drag coefficient $B$ ( $10^{-5}$ Pa s)	Burgers vector $b$ ( $10^{-10}$ m)	Young modulus $E$ (GPa)	Poisson ration $\nu$	Time step $\Delta t$ (s)
4.86	358	0.5	1	34	2.54	210	0.3	$10^{-10}$

**TABLE III:** The different DD simulation setup cases treated in this work.

Grain 1	Grain 2	Grain 3
$D_g = 1 \mu\text{m}$	$D_g = 2 \mu\text{m}$	$D_g = 2 \mu\text{m}$
z-axis = (100)	z-axis = (100)	z-axis = ( $\bar{1}54$ )

stress field and accompanying the formation of the substructure, during DD simulations of bainitic ferritic grains [35]. Further evidence supporting these claims is presented in Ref. 67, where the grain shape effect on the plastic response has been investigated in detail. The use of small cubic grain is thus preferred for the sake of minimizing the computational load.

Neutron irradiation generates small, mobile defects that later form various types of defect clusters, including interstitial dislocation loops. At room temperature, those loops are trapped by impurities and act as immobile obstacles, with respect to mobile dislocations. In the present simulations, the defect clusters are implemented in the form of planar, square-shaped surfaces called facets, oriented normal to the (100) direction for simplicity. The interaction mechanism between dislocations and facets is as follows: once a dislocation contact a facet, the effective shear stress applied on the dislocation line  $\tau^*$  is compared with the critical defect strength  $\tau_{\text{defect}}$ . The mobile dislocations can cut through a given facet provided  $\tau^* > \tau_{\text{defect}}$ . The selected  $\tau_{\text{defect}}$  level is calibrated based on the MD simulation results, depending on the incoming dislocation (edge or screw) character (see Refs. 68 and 69 for details).

Additionally, the validity of this simplified dislocation/defect interaction treatment has been evaluated by comparison with detailed DD simulation setups including actual prismatic loops [70, 71]. It is found that in the presence of cross-slip, the effective defect interaction strength and corresponding dislocation velocity are fully consistent with the MD-observed interaction mechanisms. This conclusion holds true even though the facet/defects have no associated stress field.

Uniaxial tension is applied along the (100) direction under strain rate-controlled loading conditions with  $\dot{\epsilon} = 100 \text{ s}^{-1}$ . Different irradiation conditions are simulated by inserting different defect number densities ( $5 \times 10^{20}$ – $2 \times 10^{21} \text{ m}^{-3}$ ) and defect sizes (15 and 25 nm) [2, 3, 40]. Simulations with grain sizes of 1  $\mu\text{m}$  (Grain 1 in Table III) and 2  $\mu\text{m}$  (Grain 2 and Grain 3 in Table III) have been carried out. Grain 2 and Grain 3 have two different crystallographic orientations: in the first case (Grain 2), the grain z-axis is orientated along the (100) direction. In the second case (Grain 3), the grain z-axis is orientated along the ( $\bar{1}54$ ) direction. In all the cases, the initial dislocation sources belong to the  $a/2$  (101)[ $\bar{1}\bar{1}1$ ] SS, associated with cross-slip systems  $a/2$  ( $\bar{1}\bar{1}0$ )[ $\bar{1}\bar{1}1$ ] and  $a/2$  (011)[ $\bar{1}\bar{1}1$ ]. The Schmid factors corresponding to the two selected crystallographic orientations are indicated in Table IV.

**TABLE IV:** Schmid factors acting in the different SS submitted to a (100) tensile loading for the different DD simulations cases tested in this work.

SS label	First SS	Second SS	Third SS
SS	(101)[ $\bar{1}\bar{1}1$ ]	( $\bar{1}\bar{1}0$ )[ $\bar{1}\bar{1}1$ ]	(011)[ $\bar{1}\bar{1}1$ ]
$z = (100)$ Grain 1, 2	0.41	0.41	0
$z = (\bar{1}54)$ Grain 3	0.378	0.472	0.095

### Defect-induced changes of effective dislocation mobility and DIAT shift concept

The implemented facet (loop) dispersions act as obstacles to the dislocation motion, thus affecting the effective mobility of the screw dislocation populations. The dislocation mobility change due to a given defect dispersion can be characterized by an indicator called the  $\Delta\text{DIAT}$  at a fixed straining temperature. This concept derives from the radiation-induced shift of the  $\Delta\text{DBTT}$ , usually defined for a fixed impact energy (or fracture toughness) level [19]. The  $\Delta\text{DIAT}$  level associated with a given defect dispersion is calculated as explained below:

Step 1: A DD simulation is carried out in a defect-free grain, at  $T = 300 \text{ K}$ , up to a reference plastic strain level (identified with subscript 0). The average stress  $\bar{\tau}_0^*$  and corresponding velocity  $\bar{v}_0$  levels are calculated first, accounting for all the screw dislocation segments generated during the simulation. In the absence of defect clusters, it can be shown that  $\bar{v}_0$  is a (quasi) linear function of  $\bar{\tau}_0^*$ .

Step 2: Irradiated grains including different defect dispersions (identified with subscript 1) are then strained to the same reference level for the sake of obtaining the effective resolved shear stress  $\tau_1^*$  and corresponding velocity  $v_1$  at the same straining temperature  $T = 300 \text{ K}$ . It is important to note that exactly the same dislocation mobility rule is used in both irradiated and non-irradiated cases, yielding the following relation:

$$\frac{\bar{v}_0}{v_1} \left( \frac{\tau_1^*}{\bar{\tau}_0^*} \right)^{3/2} = \exp \left( \frac{\Delta G_1(\tau_1^*)}{2k_B T_1} - \frac{\Delta G_0(\bar{\tau}_0^*)}{2k_B T_0} \right) \quad (4)$$

An apparent straining temperature  $T_1$  can be obtained by solving Eq. (4), yielding the effective straining temperature shift  $\Delta T = (T_0 - T_1)$  for the considered (screw) segment.

Step 3: For a given defect dispersion, repeating the step 2 for all screw dislocation segments can obtain a distribution of  $\Delta T$ . The  $\Delta\text{DIAT}$  level represents the most typical  $\Delta T$  variation and is thus statistically calculated as follows:

$$\Delta\text{DIAT}_{\text{sim}} = \sum_{\tau^*=\tau_{\text{min}}^*}^{\tau_{\text{max}}^*} \left[ \sum_{L=L_{\text{min}}}^{L_{\text{max}}} \Delta T(L, \tau^*) p(L, \tau^*) \right] \quad (5)$$

where  $\tau^*$  is the effective resolved shear stress acting on a given screw segment and  $p(L, \tau^*)$  is the corresponding probability of



occurrence of a given  $\Delta T$  amplitude. It can be shown that the proposed  $\Delta DIAT$  calculation method is independent of the selected reference strain level.

The present  $\Delta DIAT$  concept does not imply that dislocation interaction with dispersed obstacles and thermally activated lattice friction are actually the same physical mechanisms. It implies that dislocation/defect interactions are, however, equivalent to a definite temperature reduction, in terms of statistical, thermally activated (screw) dislocation velocities. From the author's standpoint, this defect/temperature equivalency can greatly facilitate the prediction of dose-dependent brittle–ductile transition temperature shifts, based on observation results (see also “The  $\Delta DIAT$  versus  $\Delta DBTT$  correlation”).

To the best of the author's knowledge, there is currently no experimental technique enabling direct evaluation of dislocation population mobility, let alone their characteristic, dose-dependent evolution. An atomic-scale model has been recently developed, however, explaining the brittle–ductile transition based on isolated dislocation/obstacle interaction cases [72]. This model confirms that defect-induced dislocation mobility evolutions can help revealing/evaluating the brittle–ductile transition evolutions.

## Acknowledgments

This project has received funding from the Euratom Research and Training Programme 2014–2018 under Grant Agreement No. 661913 “SOTERIA”. The views and opinions expressed herein do not necessarily reflect those of the European Commission. The support of Foundation for Youth Innovation Talents in Education Department of Guangdong (2016KQNCX005) and Guangdong Provincial key S & T Special Project (2017B020235001) is also acknowledged.

## References

1. **E.E. Bloom:** The challenge of developing structural materials for fusion power systems. *J. Nucl. Mater.* **258**, 7–17 (1998).
2. **M. Matijasevic, E. Lucon, and A. Almazouzi:** Behavior of ferritic/martensitic steels after n-irradiation at 200 and 300 °C. *J. Nucl. Mater.* **377**, 101–108 (2008).
3. **M. Matijasevic, W. Van Renterghem, and A. Almazouzi:** Characterization of irradiated single crystals of Fe and Fe–15Cr. *Acta Mater.* **57**, 1577–1585 (2009).
4. **N. Baluc, D.S. Gelles, S. Jitsukawa, A. Kimura, R.L. Klueh, G.R. Odette, B. van der Schaaf, and J. Yu:** Status of reduced activation ferritic/martensitic steel development. *J. Nucl. Mater.* **367**, 33–41 (2007).
5. **A. Hishinuma, A. Kohyama, R.L. Klueh, D.S. Gelles, and K. Ehrlich:** Current status and future R & D for reduced-activation ferritic/martensitic steels. *J. Nucl. Mater.* **258**, 193–204 (1998).
6. **Y.A. Nikolaev, A.V. Nikolaeva, and Y.I. Shtrombakh:** Radiation embrittlement of low-alloy steels. *Int. J. Pressure Vessels Piping* **79**, 619–636 (2002).
7. **M.J. Konstantinovic, W. Rebterghem, M. Matijasevic, B. Minov, M. Lambrecht, T. Toyama, M. Chiapetto, and L. Maleraba:** Mechanical and microstructural properties of neutron irradiated Fe–Cr–C alloys. *Int. J. Energy Res.* **01**, 2988–2994 (2016).
8. **H. Hein, E. Keim, J. May, and H. Schnabel:** Some Recent Research Results and Their Implications for RPV Irradiation Surveillance under Long Term Operation, IAEA Technical Meeting on Degradation of Primary Components of Pressurized Water Cooled Nuclear Power Plants, 5–8 November 2013, Vienna, Austria.
9. **E. Hintsala, C. Teresi, A.J. Wagner, K.A. Mkhoyan, and W. Gerberich:** Fracture transitions in iron: Strain rate and environmental effect. *J. Mater. Res.* **29**, 1513–1521 (2014).
10. **H. Yoo, N. Lee, T. Ham, and J. Seo:** Methodology for analyzing risk at nuclear facilities. *Ann. Nucl. Energy* **81**, 213–218 (2015).
11. **A. Ballesteros, E. Altstadt, F. Gillemot, H. Hein, J. Wagemans, J. Rouden, J. Barthelmes, K. Wilford, M. Serrano, M. Brumovsky, R. Chaouadi, and S. Ortner:** Monitoring radiation embrittlement during life extension periods. *Nucl. Eng. Des.* **267**, 197–206 (2014).
12. **E. Altstadt, E. Keim, H. Hein, M. Serrano, F. Bergner, H.W. Viehriig, A. Ballesteros, R. Chaouadi, and K. Wilford:** FP7 Project LONGLIFE: Overview of results and implications. *Nucl. Eng. Des.* **278**, 753–757 (2014).
13. **M. Diaz-Fuentes, A. Iza-Mendia, and I. Gutierrez:** Analysis of different acicular ferrite microstructures in low-carbon steels by electron backscattered diffraction. Study of their toughness behavior. *Metall. Mater. Trans. A* **34**, 2505–2516 (2003).
14. **E. Meslin, M. Lambrecht, M. Hernandez-Mayoral, F. Bergner, L. Malerba, P. Pareige, B. Radiguet, A. Barbu, D. Gómez-Briceño, A. Ulbricht, and A. Almazouzi:** Characterization of neutron-irradiated ferritic model alloys and a RPV steel from combined APT, SANS, TEM and PAS analyses. *J. Nucl. Mater.* **406**, 73–83 (2010).
15. **C. Heintze, A. Ulbricht, F. Bergner, and H. Eckerlebe:** SANS investigation of neutron-irradiated Fe–Cr alloys. *J. Phys.: Conf. Ser.* **247**, 012035 (2010).
16. **A.S. Budiman, N. Tamura, B.C. Valek, K. Gadre, J. Maiz, R. Spolenak, W.D. Nix, and J.R. Patel:** Crystal plasticity in Cu damascene interconnect lines undergoing electromigration as revealed by synchrotron X-ray microdiffraction. *Appl. Phys. Lett.* **88**, 233515 (2006).
17. **C.Y. Khoo, H. Liu, W. Sasangka, R.I. Made, N. Tamura, M. Kunz, A.S. Budiman, C.L. Gan, and C.V. Thompson:** Impact of deposition conditions on the crystallization kinetics of amorphous GeTe films. *J. Mater. Sci.* **51**, 1864–1872 (2016).
18. **S.K. Tippabhotla, I. Radchenko, W.J.R. Song, G. Illya, V. Handara, M. Kunz, N. Tamura, A.A.O. Tay, and**

- A.S. Budiman:** From cells to laminate: Probing and modeling residual stress evolution in thin silicon photovoltaic modules using synchrotron X-ray micro-diffraction experiments and finite element simulations. *Prog. Photovoltaics Res. Appl.* **25**, 791–809 (2017).
19. **Y. Li and C. Robertson:** Irradiation defect dispersions and effective dislocation mobility in strained ferritic grains: A statistical analysis based on 3D dislocation dynamics simulations. *J. Nucl. Mater.* **504**, 84–93 (2018).
  20. **Y. Li, C. Robertson, X. Ma, and B. Wang:** Investigation of radiation temperature and straining temperature effects on the screw dislocation mobility evolution in irradiated ferritic grains using 3D dislocation dynamics. In *TMS 2019 148th Annual Meeting & Exhibition Supplemental Proceedings* (Springer, Cham, 2019); pp. 1335–1344.
  21. **R.C. Birtcher, M.A. Kirk, K. Furuya, G.R. Lumpkin, and M.O. Ruault:** In situ transmission electron microscopy investigation of radiation effects. *J. Mater. Res.* **20**, 1654–1683 (2005).
  22. **J.S. Robach, I.M. Robertson, B.D. Wirth, and A. Arsenlis:** In situ transmission electron microscopy observations and molecular dynamics simulations of dislocation-defect interactions in ion-irradiated copper. *Philos. Mag.* **83**, 955–967 (2003).
  23. **D.J. Bacon and Y.N. Osetsky:** Modelling dislocation–obstacle interactions in metals exposed to an irradiation environment. *Mater. Sci. Eng., A* **400**, 353–361 (2005).
  24. **T.D. de la Rubia, H.M. Zbib, T.A. Kraishin, B.D. Wirth, M. Victoria, and M.J. Caturla:** Multiscale modelling of plastic flow localization in irradiation materials. *Nature* **406**, 871–874 (2000).
  25. **J. Kwon, S.C. Kwon, and J.H. Hong:** Prediction of radiation hardening in reactor pressure vessel steel based on a theoretical model. *Ann. Nucl. Energy* **30**, 1549–1559 (2003).
  26. **N.M. Ghoniem, S.H. Tong, B.N. Singh, and L.Z. Sun:** On dislocation interaction with radiation-induced defect clusters and plastic flow localization in fcc metals. *Philos. Mag. A* **81**, 2743–2764 (2001).
  27. **J. Chaussidon, C. Robertson, D. Rodney, and M. Fivel:** Dislocation dynamics simulations of plasticity in Fe laths at low temperature. *Acta Mater.* **56**, 5466–5476 (2008).
  28. **K. Gururaj, C. Robertson, and M. Fivel:** Post-irradiation plastic deformation in bcc Fe grains investigated by means of 3D dislocation dynamics simulations. *J. Nucl. Mater.* **459**, 194–204 (2015).
  29. **R.L. Klueh, M.A. Sokolov, K. Shiba, Y. Miwa, and J.P. Robertson:** Embrittlement of reduced-activation ferritic/martensitic steels irradiated in HFIR at 300 °C and 400 °C. *J. Nucl. Mater.* **283**, 478–482 (2000).
  30. **P.B. Hirsch and S.G. Roberts:** Modelling plastic zones and the brittle–ductile transition. *Philos. Trans. R. Soc., A* **355**, 1991 (1997).
  31. **M. Tanaka, E. Tarleton, and S.G. Roberts:** The brittle–ductile transition in single-crystal iron. *Acta Mater.* **56**, 5123–5129 (2008).
  32. **H-W. Viehrig, J. Boehmert, and J. Dzegan:** Some issues by using the master curve concept. *Nucl. Eng. Des.* **212**, 115–124 (2002).
  33. **J. Boehmert and G. Muller:** Thermally activated deformation of irradiated reactor pressure vessel steel. *J. Nucl. Mater.* **301**, 227–232 (2002).
  34. **E.N. Hahn and M.A. Meyers:** Grain-size dependent mechanical behavior of nanocrystalline metals. *Mater. Sci. Eng., A* **646**, 101–134 (2015).
  35. **C. Robertson and K. Gururaj:** Plastic deformation of ferritic grains in presence of ODS particles and irradiation-induced defect clusters: A 3D dislocation dynamics simulation study. *J. Nucl. Mater.* **415**, 167–178 (2011).
  36. **J. Chaussidon, C. Robertson, and M. Fivel:** Internal stress evolution in Fe laths deformed at low temperature analysed by dislocation dynamics simulations. *Modell. Simul. Mater. Sci. Eng.* **18**, 025003 (2010).
  37. **F. Louchet and H. Saka:** Comments on the paper: Observation of dislocation dynamics in the electron microscope by B.W. Lagow et al. *Mater. Sci. Eng., A* **352**, 71–75 (2003).
  38. **K. Gururaj, C. Robertson, and M. Fivel:** Channel formation and multiplication in irradiated FCC metals: A 3D dislocation dynamics investigation. *Philos. Mag.* **95**, 1368–1389 (2015).
  39. **C.F. Robertson, K. Obrtlik, and B. Marini:** Dislocation structures in 16MND5 pressure vessel steel strained in uniaxial tension at different temperatures from 196 °C up to 25 °C. *J. Nucl. Mater.* **366**, 58–69 (2007).
  40. **M. Rieth, B. Dafferner, and H.D. Rohrig:** Embrittlement behaviour of different international low activation alloys after neutron irradiation. *J. Nucl. Mater.* **258**, 1147–1152 (1998).
  41. **M. Rieth, S.L. Dudarev, S.M. Gonzalez de Vicente, J. Aktaa, T. Ahlgren, S. Antusch, D.E.J. Armstrong, M. Balden, N. Baluc, M.-F. Barthe, W.W. Basuki, M. Battabyal, C.S. Becquart, D. Blagoeva, H. Boldyryeva, J. Brinkmann, M. Celino, L. Ciupinski, J.B. Correia, A. De Backer, C. Domain, E. Gaganidze, C. Garcia-Rosales, J. Gibson, M.R. Gilbert, S. Giusepponi, B. Gludovatz, H. Greuner, K. Heinola, T. Höschen, A. Hoffmann, N. Holstein, F. Koch, W. Krauss, H. Li, S. Lindig, J. Linke, C. Linsmeier, P. López-Ruiz, H. Maier, J. Matejcek, T.P. Mishra, M. Muhammed, A. Muñoz, M. Muzyk, K. Nordlund, D. Nguyen-Manh, J. Opschoor, N. Ordás, T. Palacios, G. Pintsuk, R. Pippan, J. Reiser, J. Riesch, S.G. Roberts, L. Romaner, M. Rosiński, M. Sanchez, W. Schulmeyer, H. Traxler, A. Ureña, J.G. van der Laan, L. Veleva, S. Wahlberg, M. Walter, T. Weber, T. Weitkamp, S. Wurster, M.A. Yar, J.H. You, and A. Zivelonghi:** Recent progress in research on tungsten materials for nuclear fusion applications in Europe. *J. Nucl. Mater.* **432**, 482–500 (2013).
  42. **Y. Nishiyama, K. Fukaya, M. Suzuki, and M. Eto:** Irradiation embrittlement of 2 1/4Cr–1Mo steel at 400 °C and its electrochemical evaluation. *J. Nucl. Mater.* **258–263**, 1187–1192 (1998).
  43. **S.I. Porollo, A.M. Dvoriashin, A.N. Vorobyev, and Y.V. Konobeev:** The microstructure and tensile properties of Fe–Cr

- alloys after neutron irradiation at 400 C to 5.5–7.1 dpa. *J. Nucl. Mater.* **256**, 247–253 (1998).
44. **M.M. Ghoniem and F.H.ammad:** Pressure vessel steels: Influence of chemical composition on irradiation sensitivity. *Int. J. Pressure Vessels Piping* **74**, 189 (1997).
  45. **E.A. Kuleshova, B.A. Gurovich, Y.I. Shtrombakh, D.Y. Erak, and O.V. Lavrenchuk:** Comparison of microstructural features of radiation embrittlement of VVER-440 and VVER-1000 reactor pressure vessel steels. *J. Nucl. Mater.* **300**, 127–140 (2002).
  46. **J. Kocik, E. Keilova, J. Cizek, and I. Prochazka:** TEM and PAS study of neutron irradiated VVER-type RPV steels. *J. Nucl. Mater.* **303**, 52–64 (2002).
  47. **X. Jia and Y. Dai:** Microstructure in martensitic steels T91 and F82H after irradiation in SINQ target-3. *J. Nucl. Mater.* **318**, 207–214 (2003).
  48. **S.M. Bruemmer, E.P. Simonen, P.M. Scrott, P.L. Andresen, G.S. Was, and J.L. Nelson:** Radiation-induced material changes and susceptibility to intergranular failure of light-water-reactor core internals. *J. Nucl. Mater.* **274**, 299–314 (1999).
  49. **P. Forget, B. Marini, and L. Vincent:** Application of local approach to fracture of an RPV steel: Effect of the crystal plasticity on the critical carbide size. *Procedia Struct. Integr.* **2**, 1660–1667 (2016).
  50. **T.L. Anderson, D. Steinstra, and R.H. Dodds:** A theoretical framework for addressing fracture in the ductile–brittle transition region. *Fract. Mech.* **24**, 185 (1994).
  51. **L. Vincent, M. Libert, B. Marini, and C. Rey:** Towards a modelling of RPV steel brittle fracture using crystal plasticity computations on polycrystalline aggregates. *J. Nucl. Mater.* **406**, 91–96 (2010).
  52. **M. Liber, C. Rey, L. Vincent, and B. Marini:** Temperature dependent poly-crystal model application to bainitic steel behavior under tri-axial loading in the ductile–brittle transition. *Int. J. Solids Struct.* **48**, 2196–2208 (2011).
  53. **P. Forget, B. Marini, A. Parrot, and P. Todeschini:** Numerical evaluation of the ability of the master curve approach to described the effect of irradiation on the brittle fracture toughness of RPV steels. In *Local Approach to Fracture*, J. Besson, D. Moinereau, and D. Steglich, eds. (Ecole des Mines de Paris, Paris, 2006); pp. 297–303.
  54. **M.A. Sokolov, R.K. Nanstad, and M.K. Miller:** Fracture toughness and atom probe characterization of a highly embrittled RPV weld. *J. ASTM Int.* **1**, 1–15 (2004).
  55. **G.S. Was:** *Fundamentals of Radiation Materials Science*, 1st ed. (Springer Berlin Heidelberg, New York, 2007).
  56. **M. Yamaguchi:** First-principles study on the grain boundary embrittlement of metals by solute segregation: Part I. Iron (Fe)-solute (B, C, P, and S) systems. *Metall. Mater. Trans. A* **42**, 319–329 (2011).
  57. **M. Verdier, M. Fivel, and I. Groma:** Mesoscopic scale simulation of dislocation dynamics in fcc metals: Principles and applications. *Modell. Simul. Mater. Sci. Eng.* **6**, 755 (1998).
  58. **M. Tang, L.P. Kubin, and G.R. Canova:** Dislocation mobility and the mechanical response of bcc single crystals: A mesoscopic approach. *Acta Mater.* **46**, 3221–3235 (1998).
  59. **D. Caillard and J.L. Martin:** *Thermally Activated Mechanisms in Crystal Plasticity*, 1st ed. (Elsevier, Kidlington, 2003).
  60. **M.R. Gilbert, P. Schuck, B. Sadigh, and J. Marian:** Free energy generalization of the peierls potential in iron. *Phys. Rev. Lett.* **111**, 095502 (2013).
  61. **C.R. Weinberger, B.L. Boyce, and C.C. Bataille:** Slip planes in bcc transition metals. *Int. Mater. Rev.* **58**, 296–314 (2013).
  62. **V.I. Alshits and V.L. Indenbom:** Mechanisms of dislocation drag. In *Dislocations in Solids*, Vol. 7, F.R.N. Nabarro, ed. (Elsevier, Amsterdam, 1986); ch. 34, pp. 43–111.
  63. **B. Gurrutxaga-Lerma, M.A. Shehadeh, D.S. Balint, D. Dini, L. Chen, and D.E. Eakins:** The effect of temperature on the elastic precursor decay in shock loaded FCC aluminium and BCC iron. *Int. J. Plast.* **96**, 135–155 (2017).
  64. **M.R. Gilbert, S. Queyreau, and J. Marian:** Stress and temperature dependence of screw dislocation mobility in  $\alpha$ -Fe by molecular dynamics. *Phys. Rev. B* **84**, 174103 (2011).
  65. **G. Po, Y. Cui, D. Rivera, D. Cereceda, T.D. Swinburne, J. Marian, and N. Ghoniem:** A phenomenological dislocation mobility law for bcc metals. *Acta Mater.* **119**, 123–135 (2016).
  66. **D. Garcia-Rodriguez:** Optimisation d'un code de dynamique des dislocations pour l'étude de la plasticité des aciers ferritiques. Doctoral dissertation, Université de Grenoble, Grenoble, 2011.
  67. **M. Jiang, B. Devincere, and G. Monnet:** Effects of the grain size and shape on the flow stress: A dislocation dynamics study. *Int. J. Plast.* **113**, 111–124 (2019).
  68. **D. Terentyev, D.J. Bacon, and Y.N. Osetsky:** Reactions between a  $1/2 \langle 111 \rangle$  screw dislocation and  $\langle 100 \rangle$  interstitial dislocation loops in alpha-iron modelled at atomic scale. *Philos. Mag.* **90**, 1019–1033 (2010).
  69. **D. Terentyev, P. Grammatikopoulos, D.J. Bacon, and Y.N. Osetsky:** Simulation of the interaction between an edge dislocation and a  $\langle 100 \rangle$  interstitial dislocation loop in  $\alpha$ -iron. *Acta Mater.* **56**, 5034–5046 (2008).
  70. **Y. Li, C. Robertson, M. Shukeir, and L. Dupuy:** Screw dislocation interaction with irradiation defect-loops in  $\alpha$ -iron: Evaluation of cross-slip effect using dislocation dynamics simulations. *Modell. Simul. Mater. Sci. Eng.* **26**, 055009 (2018).
  71. **Y. Li, C. Robertson, M. Shukeir, and L. Dupuy:** Screw dislocation interaction with irradiation defect-loops in  $\alpha$ -iron: Evaluation of loop-induced stress field effect using dislocation dynamics simulations. *Nucl. Instrum. Methods Phys. Res., Sect. B* (2019). (in press) <https://doi.org/10.1016/j.nimb.2019.01.032>.
  72. **T.D. Swinburne and S.L. Dudarev:** Kink-limited Orowan strengthening explains the brittle to ductile transition of irradiated and unirradiated bcc metals. *Phys. Rev. Mater.* **2**, 073608 (2018).